

Spatial Resolution Matching of Microwave Radiometer Measurements Using Iterative Deconvolution with Close Loop Priors (ICLP)

Yao, Zhiyu; Hu, Weidong; Feng, Zhiyan; Zhang, Wenlong; Liu, Yang; Xu, Zhihao; Ligthart, Leo P.

DOI

10.1109/TGRS.2023.3291752

Publication date

Document Version Final published version

Published in

IEEE Transactions on Geoscience and Remote Sensing

Citation (APA)
Yao, Z., Hu, W., Feng, Z., Zhang, W., Liu, Y., Xu, Z., & Ligthart, L. P. (2023). Spatial Resolution Matching of Microwave Radiometer Measurements Using Iterative Deconvolution with Close Loop Priors (ICLP). IEEE Transactions on Geoscience and Remote Sensing, 61, 1-14. Article 5301614. https://doi.org/10.1109/TGRS.2023.3291752

Important note

To cite this publication, please use the final published version (if applicable). Please check the document version above.

Copyright

Other than for strictly personal use, it is not permitted to download, forward or distribute the text or part of it, without the consent of the author(s) and/or copyright holder(s), unless the work is under an open content license such as Creative Commons.

Please contact us and provide details if you believe this document breaches copyrights. We will remove access to the work immediately and investigate your claim.

Spatial Resolution Matching of Microwave Radiometer Measurements Using Iterative Deconvolution With Close Loop Priors (ICLP)

Zhiyu Yao[®], Weidong Hu[®], Zhiyan Feng[®], Wenlong Zhang[®], Yang Liu[®], Zhihao Xu[®], and Leo P. Ligthart[®], *Life Fellow, IEEE*

Abstract—Passive multifrequency microwave sensors frequently struggle with difficulties of nonuniform spatial resolution among multiple channels. The raw measurements in the land-sea transition zone are seriously contaminated. Conventional analytical deconvolution techniques suffer from the tradeoff between spatial resolution enhancement and noise amplification, leading to low data integrity in the practical spatial resolution matching application. To provide multichannel microwave radiometer (MWR) data with matching levels of spatial resolution, a method based on iterative deconvolution with close loop priors (ICLP) is proposed. Specifically, a destriping module is first utilized as a preprocessing step to maintain high data integrity. Then, the close loop mechanism using sparse adaptive priors is proposed to balance the spatial resolution and data integrity enhancement. Also, progressively iterative deconvolution is introduced to realize controllable levels of spatial resolution enhancement (spatial resolution matching) for multichannel data to reach a consistent level. Experiments performed using both simulated and actual microwave radiation imager (MWRI) data demonstrate the validity and effectiveness of the method.

Index Terms—Close loop, FengYun-3-D (FY-3D), iterative deconvolution, microwave radiation imager (MWRI), priors, spatial resolution matching.

I. INTRODUCTION

ICROWAVE radiometer (MWR) is designed to obtain radiometric measurements with a combination of frequency and polarization [1]. Due to the continuous, all-weather, all-day observing capabilities, the MWR has been extensively employed in worldwide weather parameters monitoring [2]. The retrieval of meteorological parameters, such as cloud liquid water, total precipitation water, sea wind speed, snow depth, and snow water equivalent, relies tremendously on the MWR instrument [3], [4], [5].

Manuscript received 5 January 2023; revised 18 May 2023; accepted 28 June 2023. Date of publication 3 July 2023; date of current version 13 July 2023. This work was supported in part by the National Natural Science Foundation of China under Grant 61527805 and Grant 61731001. (Corresponding author: Weidong Hu.)

Zhiyu Yao, Weidong Hu, Zhiyan Feng, and Zhihao Xu are with the School of Integrated Circuits and Electronics, Beijing Institute of Technology, Beijing 100081, China (e-mail: hoowind@bit.edu.cn).

Wenlong Zhang is with the Department of Computing, The Hong Kong Polytechnic University, Hong Kong.

Yang Liu is with the Aerospace Information Research Institute, Chinese Academy of Sciences, Beijing 100864, China.

Leo P. Ligthart is with the Faculty of Electrical Engineering, Delft University of Technology, 2628 CN Delft, The Netherlands.

Digital Object Identifier 10.1109/TGRS.2023.3291752

Overall, the MWR's global observations are inevitably hampered by low and nonuniform spatial resolution. Furthermore, the local data in the land–sea transition zone are severely contaminated by the relatively sizeable measured footprint covering both terrestrial and ocean [6], [7], [8], leading to poor local data integrity. To match to lower-frequency channels with a low spatial resolution for multichannel joint retrieval, one common strategy is to average high-frequency channel data with a high spatial resolution [9], [10]. However, the multifrequency channel data with the finer spatial resolution are desperate to be obtained when collecting the small regional-scale distribution parameters with high-precision requirements [11].

Spatial resolution matching aims to enhance low-frequency channel data with low resolution to up-match high-frequency channel data with high resolution, which is a special kind of controllable spatial resolution enhancement algorithm. Spatial resolution-matching algorithms are roughly categorized into three groups: antenna pattern inversion, data fusion, and learning-based methods [12], [13]. The antenna pattern inversion algorithms enhance the spatial resolution by using the redundant oversampling information from the radiometer measurement scanning mechanism, such as the Backus-Gilbert (BG) method [14], the radiometer version of the scatterometer image reconstruction (rSIR) method [15], and the iterative methods in Hilbert and Banach space [13], [16]. Data fusion techniques enhance the spatial resolution of the low-resolution (low-frequency) channels by fusing auxiliary information from the spectral imager [17] or the finer-resolution (higher frequency) channels [18], [19]. Learning-based technologies exploit the corresponding intrinsic relationship of the MWR imaging process to model an end-to-end mapping by deep networks [20], [21], [22], [23].

For global data, existing methods have achieved impressive spatial resolution enhancement results in various scenarios. However, they also face a significant problem: the noise amplification and Gibbs fluctuation deteriorate the data integrity of the land–sea interface local data [24]. Fusion- and learning-based methods rarely consider the data integrity of local data, and partial antenna pattern inversion methods can only reduce the noise amplification and Gibbs fluctuation of local data at the land–sea interface area [13], [25]. In short, few methods can simultaneously enhance both global and local data.

1558-0644 © 2023 IEEE. Personal use is permitted, but republication/redistribution requires IEEE permission. See https://www.ieee.org/publications/rights/index.html for more information.

Compared with other types of remote-sensing images, radiometer data require extracting accurate amplitude information to retrieve meteorological parameters quantitatively [8], [26]. However, the Gibbs fluctuations introduced in the resolution enhancement process can cause over-enhancement of the local data and make it difficult to reconstruct the exact amplitude. Ignoring local data integrity significantly limits the upper bound of spatial resolution enhancement for global data. Traditional enhancement methods have a tradeoff problem between spatial resolution and data integrity because they perform deconvolution and convolution operations on the Gaussian kernel, respectively, leading to a mutually constraining process. The TVBF+ method substantially improves the data integrity while obtaining similar spatial resolution [26]. Nevertheless, it only mitigates rather than improves the mutual constraints and tradeoff between spatial resolution enhancement and data integrity enhancement.

In this article, the spatial resolution matching framework based on progressively iterative deconvolution with close loop priors (ICLP) mechanism is proposed. The raw measurements are first passed through a destripe module and then input into a group of a cascaded unconstrained deconvolution module and an adaptive denoising module. Then the statistical adaptive priors information of the remote-sensing images is extracted from the output of the denoising module. Next, the spatial resolution of the raw measurements is re-enhanced by a deconvolution module constrained with the priors information, and these three modules together constitute a closed-loop feedback structure. Lastly, by cascading more constrained deconvolution modules and adaptive denoising modules to form several local closed-loop feedback, the spatial resolution matching is achieved progressively and iteratively.

The contributions of this article are summarized below.

- Before the spatial resolution matching algorithm, a stripe noise removal operation is performed. Additionally, the bilateral fusion algorithm introduces multichannel consistency constraints specific to microwave radiation imager (MWRI). These two operations collectively ensure high data integrity during the spatial resolutionmatching process.
- 2) The closed-loop feedback mechanism utilizes local enhancement (data integrity) to constrain global enhancement (spatial resolution) to address the tradeoff between spatial resolution and noise amplification and Gibbs fluctuation generation. The mutually constrained relationship between data integrity enhancement and spatial resolution enhancement is transformed into a mutually beneficial relationship.
- 3) Based on the closed-loop mechanism, progressive iterative deconvolution is designed to improve both spatial resolution and data integrity further. By adjusting the number of modules for different channels, the resolutions of multiple channels with different resolutions can be matched to the same level, thus realizing multichannel spatial resolution matching. The relevant experiments demonstrate the design of the effectiveness of the resolution-matching framework.

The rest of this article is organized as follows. In Section II, the proposed resolution-matching technique is elucidated. Experimental results and detailed analysis undertaken on both simulated and actual MWRI radiometer data are presented and discussed in Section III, while conclusions are drawn in Section IV.

II. THEORETICAL BACKGROUND

The radiometer collects radiated measurements from the Earth's surface at different frequencies and polarization. The measurements received by the antenna are universally formulated as the convolution of the actual scene brightness temperature with the normalized antenna pattern, which can be represented by [27]

$$T_A = \iint_{\Omega} G(l)T_B(l)dA + n \tag{1}$$

where l is the integration variable spanning the spatial domain Ω , T_A denotes the actual known radiometer measurements, T_B is the unknown scene brightness temperature to be reconstructed, and G is the smooth integration point spread function (PSF) which is the ground-projected footprint of the original antenna pattern due to the scan geometry. The noise n is caused by the insufficient sensitivity of the radiometer receiver.

Thus, the discretized version of (1) leads to an underdetermined linear problem [19] which can be expressed by

$$m = H \otimes f + n \tag{2}$$

where $m \in \mathbb{R}^N$ is the vector that denotes the blurry and noisy measurements T_A , $f \in \mathbb{R}^M$ is the vector that denotes the unknown image T_B that is required to be solved, $H \in \mathbb{R}^{M \times N}$ is the matrix representing a projected antenna pattern footprint, \otimes is the convolution operator, and $n \in \mathbb{R}^N$ is a vector corresponding to the radiometer system noise.

Notably, in this article, the values of M and N are set to the same for multichannel spatial resolution matching.

The data degradation of the MWR defined by (2) is an ill-posed problem, which can be solved using regularization methods [28], [29]

$$\hat{f} = \underset{f}{\arg\min} \left(\delta_m(f) + \lambda \cdot \delta_{\text{REG}}(f) \right) \tag{3}$$

where \hat{f} is the optimization objective of f, δ_m is an original data-constrained term, δ_{REG} is the penalty regularization constrained term, and λ defines the relative weights for the two terms.

As shown in Fig. 1, the complete resolution-matching framework consists of a destripe block as well as *n* deconvolution and denoising (DD) blocks. A DD block consists of a sparse adaptive priors deconvolution module and a bilateral fusion module. Deconvolution using sparse adaptive priors is a kind of nonblind deconvolution. The bilateral fusion module is cascaded into the deconvolution module to eliminate noise and Gibbs fluctuations [26]. The constraints between adjacent DD blocks are achieved by closed-loop feedback. The detailed feature of the proposed DD blocks and closed-loop feedback mechanism is described below.

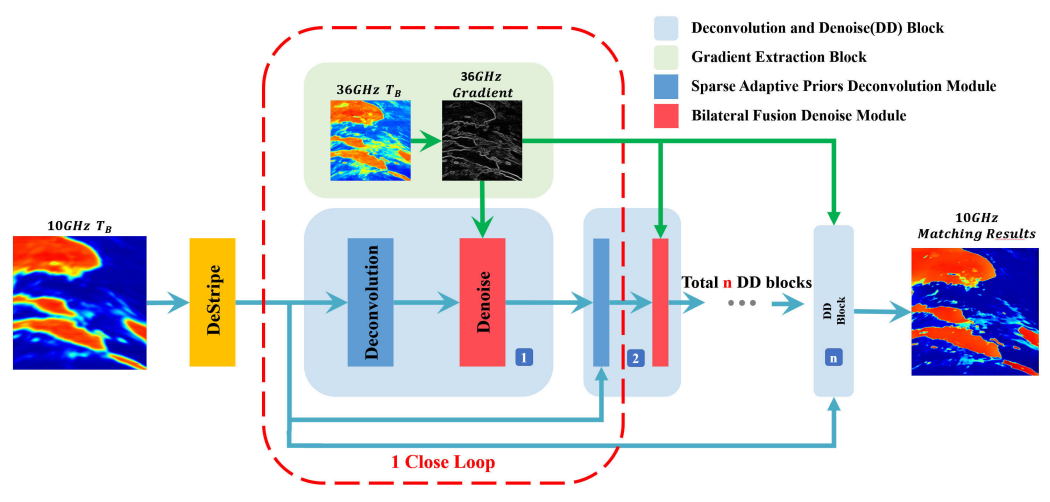


Fig. 1. Illustration of the proposed iterative deconvolution with closed-loop priors. The 10-GHz image is matched up to the 36-GHz image as a demonstration. The blocks in the red dotted box are an example of a set of closed-loop feedback.



Fig. 2. Illustration of the proposed closed-loop feedback mechanism.

A. Preprocessing of Stripe Noise Removal Before Spatial Resolution Matching

Inspired by the stripe noise removal techniques in hyperspectral image processing [30], [31], we observed significant stripe noise in MWRI data, as described in Section III-A3. Previous spatial resolution enhancement/spatial resolutionmatching algorithms have rarely addressed this issue. Therefore, we introduce a preprocessing module for stripe noise removal to ensure data integrity before performing spatialresolution matching.

B. Closed-Loop Deconvolution Using Sparse Adaptive Priors

The flow of the closed-loop deconvolution using sparse adaptive priors is implemented according to the partial block diagram in Fig. 1 (closed-loop structure part surrounded by the red dotted line). After the destriping process, the original data is initially processed through a sparse adaptive priors deconvolution module without any constraint, and the output is subsequently processed through the cascaded bilateral fusion module. Then, the derivative of one DD block's output is computed and inputted to the next DD block along with the raw measurement data. In the subsequent DD block, the original measurements' sparse adaptive priors deconvolution process is redone under the previous DD block's output constraint. In summary, the closed-loop feedback comprises a complete DD block and an additional sparse adaptive priors deconvolution module.

The essential principle of the proposed closed-loop feedback mechanism is illustrated in Fig. 2. The blue deconvolution module enclosed by the red dashed line in Fig. 1 corresponds to global enhancement in Fig. 2 and the red denoising module corresponds to local enhancement in Fig. 2.

For the radiometer data, the sparse adaptive prior deconvolution is a kind of global enhancement used to improve spatial resolution. On the other hand, bilateral fusion is a type of local enhancement of the land–sea interface region to enhance data integrity. In this article, the closed-loop feedback mechanism is introduced to exploit the sparse distribution characteristics of the microwave image derivatives. The statistical priors [32], [33], [34] of microwave remote-sensing images can be extracted as fused information to avoid interference caused by different behaviors of different channels.

Therefore, considering the local data at the land-sea boundary as a critical factor, the method is proposed to simultaneously enhance the spatial resolution and data integrity.

- The original data is enhanced globally by an unconstrained traditional deconvolution module. At this stage, noise amplification and the generation of Gibbs oscillations occur simultaneously.
- 2) A bilateral fusion algorithm is cascaded after the traditional deconvolution module to impose spatial consistency constraints on multifrequency channels, which enables local enhancement of the coastal transition zone data based on the first global enhancement and thus improves data integrity.
- 3) After the original data is globally enhanced once and locally enhanced once, the adaptive prior information of the high-quality data obtained from bilateral fusion is extracted, and the whole image is re-enhanced under constrained conditions of global deconvolution.

These three enhancements together form one complete closed-loop feedback, aiming to improve both global and local data. Generally speaking, spatial resolution and data integrity are remarkably improved with the proposed closed-loop deconvolution using sparse adaptive priors.

In the sparse adaptive priors deconvolution, (3) can be expressed explicitly as

$$\hat{f} = \underset{f}{\arg\min} \, \delta(f)$$

$$= \underset{f}{\arg\min} \, \|hf - m\|_{2}^{2} + \sum_{s=1}^{5} \lambda_{s} \|d_{s}f - w_{s}\|_{2}^{2}$$
 (4)

where d_s represent the first- and second-order derivative filter operators: d_x , d_y , d_{xx} , d_{yy} , and d_{xy} , respectively, λ_s are the positive weights, and w_s are the specified responses of the ideal data f.

By adjusting the value of w_s , it is possible to specify the adaptive priors on the derivatives of f. Furthermore, the threshold τ is introduced to suppress noise amplification, which can be represented by

$$w_s = \varphi(d_s \hat{f}_{DD}) = \frac{d_s \hat{f}_{DD}}{\left(\frac{\tau}{d_s \hat{f}_{DD}}\right)^4 + 1}$$
 (5)

where \hat{f}_{DD} is the output of the previous DD block.

In the proposed method, we set $\tau=0.5$ for first-order derivatives and $\tau=0.35$ for second-order derivatives. The value of w_s gradually approaches 0 with $|d_s \hat{f}_{i,j}| < \tau$. Thus, the pixel with a small derivative is considered noise and selectively penalized. In contrast, the pixel with a large derivative is considered a land-sea interface which can be preserved in the proposed deconvolution algorithms.

Since $\delta(f)$ is derivable with respect to f, the solution of (4) can be calculated by taking the derivative to (4)

$$\left(h^{T}h + \sum_{s=1}^{5} \lambda_{s} d_{s}^{T} d_{s}\right) \hat{f} = h^{T}m + \sum_{s=1}^{5} \lambda_{s} d_{s}^{T} w_{s}. \tag{6}$$

The solution of \hat{f} can be solved by

$$a\hat{f} = b \tag{7}$$

where

$$a = h^T h + \sum_{s=1}^5 \lambda_s d_s^T d_s$$
 (8a)

$$b = h^T m + \sum_{s=1}^5 \lambda_s d_s^T w_s. \tag{8b}$$

However, a is the sum of antenna pattern operation and derivative operation, which can be regarded as combined convolution operators. b can be considered as the constrained measured data. The proposed method aims to reconstruct \hat{f} from the constrained measured data using combined convolution operators.

To solve the equation, we apply the Fourier transform to both sides of (7)

$$A\hat{F} = B \tag{9}$$

where

$$A = H^*H + \sum_{s=1}^{5} \lambda_s D_s^* D_s$$
 (10a)

$$B = H^T M + \sum_{s=1}^{5} \lambda_s D_s^T W_s \tag{10b}$$

where $A = \mathcal{F}(a)$, $B = \mathcal{F}(b)$, $H = \mathcal{F}(h)$, $M = \mathcal{F}(m)$, $D = \mathcal{F}(d)$, $W = \mathcal{F}(w)$, and \mathcal{F} denotes the Fourier transform operator. Then, \hat{f} can be obtained

$$\hat{f} = \mathcal{F}^{-1}(B/A). \tag{11}$$

Thus, the result of one closed-loop deconvolution using sparse adaptive priors is obtained, which reconstructs the measured data with the advantages of preserving sharp land—sea interfaces and suppressing noise amplification. With the proposed method, spatial resolution and data integrity can be enhanced simultaneously.

C. Progressively Iterative Deconvolution and Resolution Matching Strategy

Based on closed-loop priors mechanism deconvolution, the complete progressively iterative deconvolution structure is constituted (several DD blocks). An enhanced spatial resolution and data integrity image are gradually generated through progressively iterative deconvolution. The number of DD blocks is determined as follows:

$$\frac{\|\hat{f}_n - \hat{f}_{n-1}\|_2}{\|\hat{f}_{n-1}\|_2} \le \mu \tag{12}$$

where μ is the parameter that measures the similarity of \hat{f}_n and \hat{f}_{n-1} .

During the actual application of multichannel microwave data, the nonuniform spatial resolution limits the data integrity of joint multichannel geological parameter retrieval products. As shown in Fig. 3, the scene contains the Mediterranean region, where spatial resolution and the contaminated land—sea transition zone of the different channels are different. The width of the gradient variation bands, which denotes the contamination bands near the land—sea interface, is broader as the spatial resolution decrease.

Essentially, the spatial resolution-matching process of the radiometer data is a controllable spatial resolution enhancement. Using the existing method with fixed reconstructed capability, it is challenging to match the spatial resolution of all the channels to the same level, especially for 10 V/H with a large blur antenna pattern footprint. Through the proposed progressively iterative deconvolution with closed-loop priors, we can gradually match the spatial resolution of multichannel data by adjusting the number of DD blocks.

III. NUMERICAL EXPERIMENTS

In this section, some numerical experiments on simulated and real MWRI data are performed using MATLAB and Python (PyTorch framework) to discuss the reconstruction performances of the proposed ICLP versus the traditional BG inversion [14] and our early work TVBF+ method [26]. Furthermore, to demonstrate the superiority of the proposed method, the deep-learning-based method, which has been proven to be a more substantial reconstruction than the traditional analytical problem [20], [22], [23], is also used as a benchmark. In this article, we choose the basic net structure in EDSR [35] and SR main branch of radiometer spatial resolution-matching method [12] for contrast (16 layers residual block). Also, in Section III-B, several additional methods were employed to compare the performance of the algorithms on actual measurements, which are outliers [36], PMP [37], and Real-ESRGAN [38].

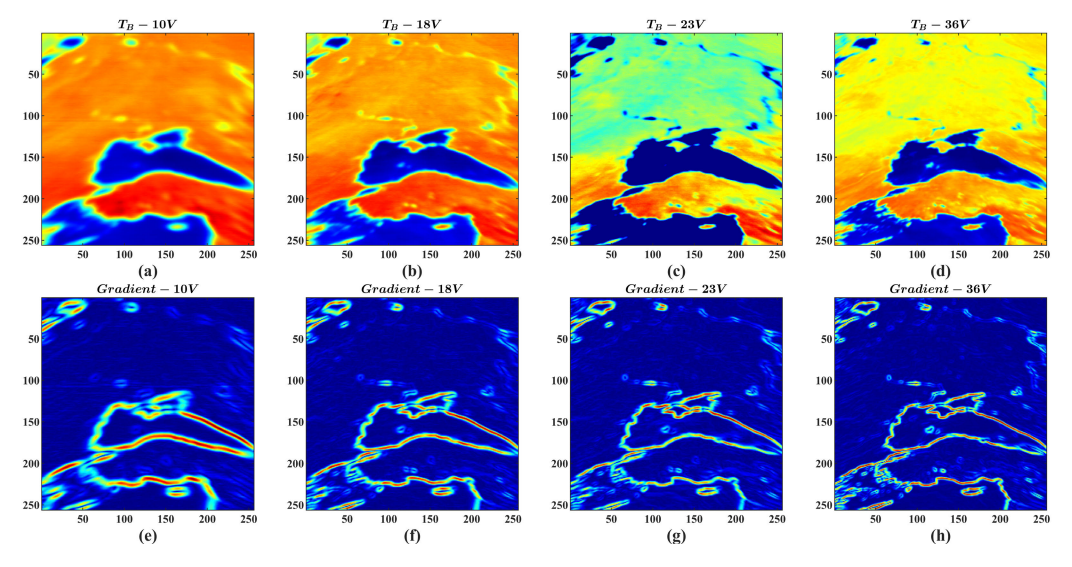


Fig. 3. Performances of the different frequency channels and the gradient calculated with the Sobel operator. Raw measurements of (a) 10 V, (b) 18 V, (c) 23 V, and (d) 36 V. Gradient of (e) 10 V, (f) 18 V, (g) 23 V, and (h) 36 V.

All the actual experimental data were obtained from the conical-scanning MWRI onboard the FengYun-3-D (FY-3D) satellite [39], which are Level-1 (L1) swath data that preserve the native scan geometry compared with gridded data [13]. The MWRI observes the Earth at an altitude of 836 km, observation of 45°, and an azimuth spanning 104°, leading to a swath width of 1400 km. It collects the Earth's surface radiation at five frequencies (10.65, 18.7, 23.8, 36.5, and 89 GHz) with vertical and horizontal polarization. For convenience, the total ten channels of MWRI are represented as 10, 18, 23, 36, and 89 V/H, respectively. The total number of measurement points is 266×1825 (the scan direction × the track direction) at each channel. The specific performances of the FY-3D MWRI instrument are compiled in Table I [1].

The ultimate ability to handle the single-channel resolution enhancement of the proposed algorithm must be illustrated before multichannel resolution-matching cases are performed. Thus, the spatial resolution enhancement of the 10 V/H channel (worst degradation case) using simulated and actual data is presented in parts Sections III-A and III-B, respectively. The spatial resolution-matching case for four channels is shown in Section III-C.

A. Spatial Resolution Enchantment on Simulated Data

Using actual MWRI data to undertake quantitative spatial resolution analysis and data integrity enhancement is complex. The inconsistent performance of the multifrequency channels exacerbates the difficulty of the problem. Thus, the simulated brightness temperature image can be a substitute. The peak signal-to-noise ratio (PSNR) [40] and structural similarity (SSIM) [41], which are widely recognized for their capacity to analyze an image in terms of the pixel level, are used as objective metrics.

1) Simulated Synthetic Data: As illustrated in Fig. 4(a), the simulation of a continental area containing abrupt discontinuities and continuously undulating land–sea interfaces is at the

center of the scenario. The gradually enlarged pairs of double lines, triple lines, and spots around the center of the scene are generated to simulate rivers and small isolated islands, representing the maximum reconstruction capability. The local areas of the small, isolated spots (enclosed by a black dashdotted rectangle), and the simulated land–sea interface area (enclosed by a white dash-dotted rectangle) are enlarged for better visual evaluation. Fig. 4(b) shows the simulated 10 V/H image generated by Fig. 4(a) and (2). The antenna pattern of the MWRI instrument system can be considered a low-pass spatial frequency filter. The simulated small islands and the land–sea interface are smoothed to disappear, as illustrated in Fig. 4(b). Fig. 4(c)–(f) depicts the reconstruction results obtained by different methods, while the related performance metrics are listed in Table II (scene 1).

As can be seen, all methods have sharper reconstructed results than the simulated 10 V/H image. Specifically, traditional BG methods enhance spatial resolution at the expense of noise amplification. The poor data integrity further limits spatial resolution enhancement. The reconstructed result of TVBF+ significantly improves data integrity while obtaining a similar spatial resolution enhancement ability as the BG method. The EDSR presents improvements in both data integrity and spatial resolution enhancement while introducing some spurious information (as the area pointed by the black arrow, the restored amplitude in the center of spots is too high). The proposed ICLP delivers phenomenal reconstructed results in data integrity and spatial resolution simultaneously. Polluted data from land—sea transition zone are apparently eliminated, and no noticeable artifacts are introduced.

Detailed analyses of the brightness temperature reconstruction performance are evaluated with the along-track transects [labeled with the green dash-dotted line in Fig. 4(a)], as shown in Fig. 5. The sharpness and amplitude of small targets in the simulated 10 V/H image are severely damaged. It is difficult to fix the worst case with conventional BG. The TVBF+ can only reconstruct the shape of the target but not the precise

Frequency	Polarization	The Instantaneous Field Of View	Sampling Interval	Integration Time	Noise
(GHz)		(km)	(km)	(km)	(K)
10.65	V/H	51×85	6×11	15.0	0.5
18.7	V/H	30×50	6×11	10.0	0.5
23.8	V/H	27×45	6×11	7.5	0.5
36.5	V/H	18×30	6×11	5.0	0.5
89	V/H	9×15	6×11	2.5	1.0

TABLE I
MAIN CHARACTERISTICS OF THE FY3D MWRI

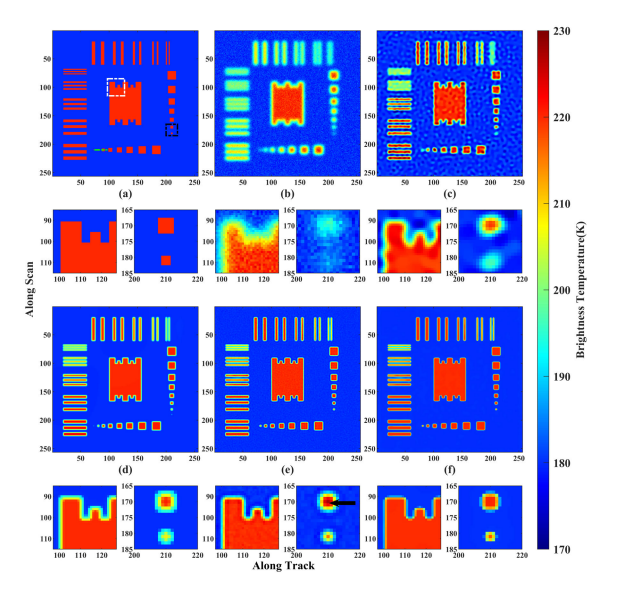


Fig. 4. (a) Synthetic brightness temperature image. (b) Simulated 10 V/H measurement obtained from Fig. 4(a). Results reconstructed from Fig. 4(b) using the (c) BG method, (d) TVBF+, (e) EDSR, and (f) ICLP.

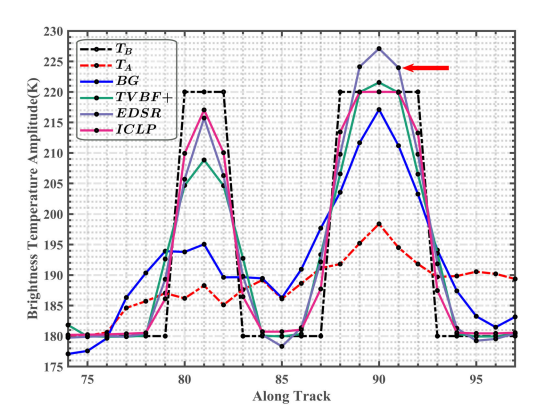


Fig. 5. Along-track transects of the synthetic scenario [labeled with the green dash-dotted line in Fig. 4(a)].

amplitude due to its limited power in resolution enhancement. The learning-based EDSR achieves a balance between spatial resolution enhancement and noise amplification to some extent. Yet, it inevitably introduces the Gibbs-related artifact (the area pointed by the red arrow) because of the irreversibly lost high-frequency information. Notably, the proposed ICLP method deals with the problem of optimal sharpness, unexpected artifact, and accurate restoration in equilibrium.

The spatial resolution can be obtained by calculating the footprint size at the nadir [10], as shown in Fig. 6. Also, the

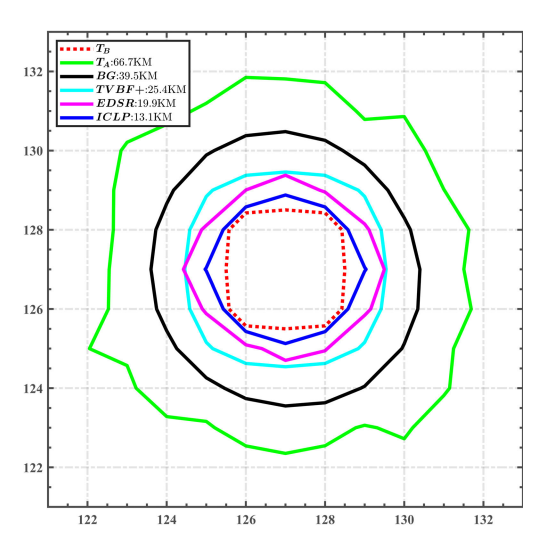


Fig. 6. Reconstructed antenna pattern footprint at nadir using the algorithm in Fig. 4(c)-(f).

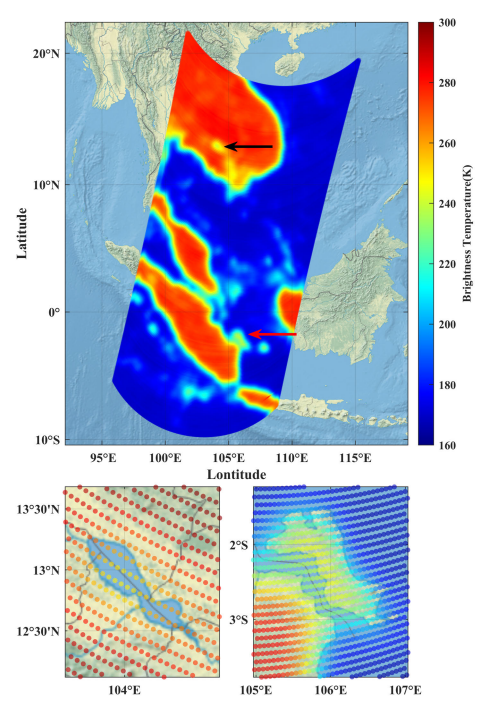


Fig. 7. Range of the experimental area on the map. (Bottom left) Enlarged area of the Tonle Sap Lake. (Bottom right) Enlarged area of the Kota Pangkalpinang. The sampling points on the map represent the position, and the color represents the brightness temperature of the measurements at the position.

quantitative spatial resolution value (SRV) can be calculated using the highest correlation coefficient proposed in LiY [12],

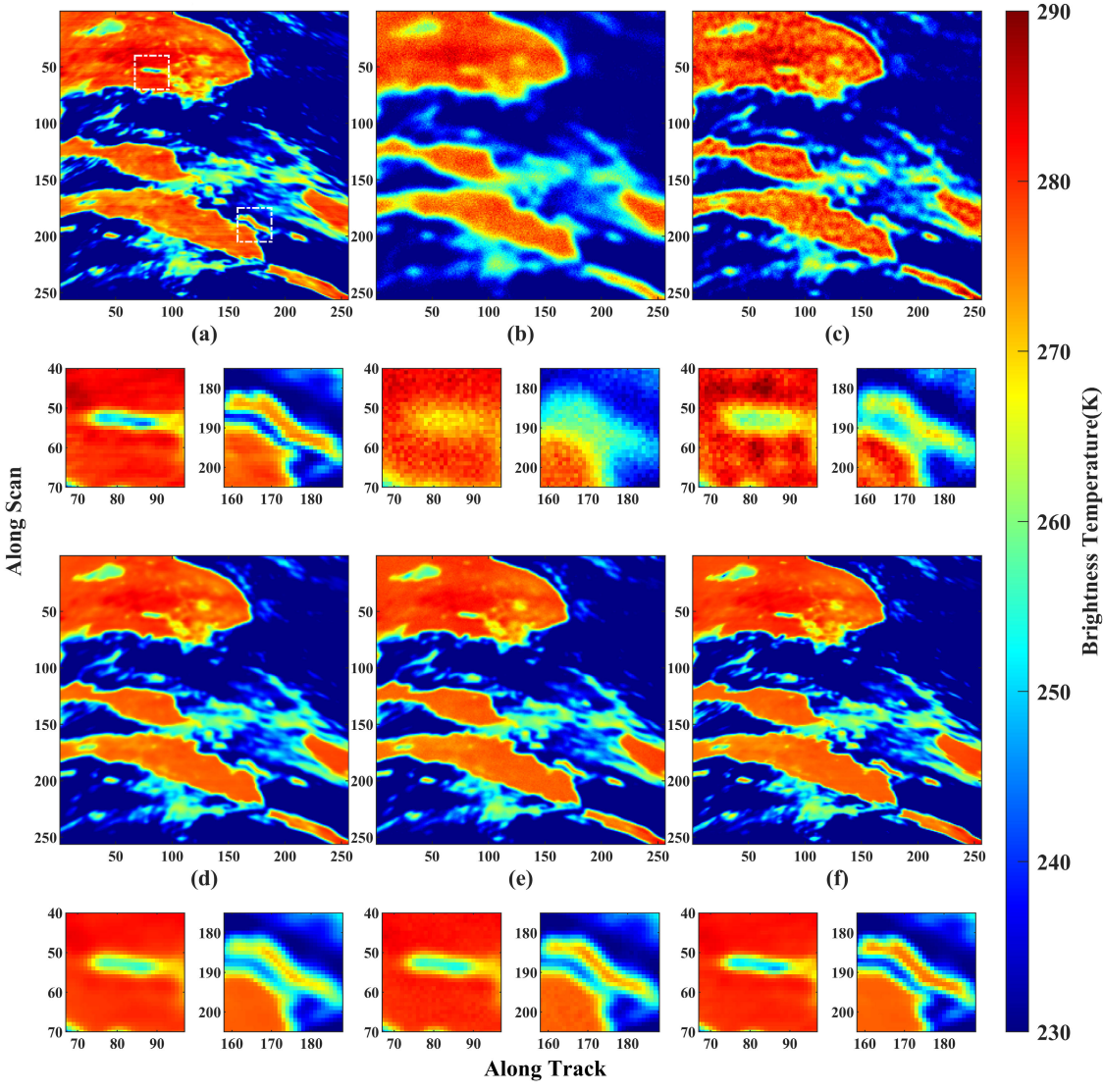


Fig. 8. (a) Synthetic scene brightness temperature image. (b) Simulated 10-V antenna brightness temperature image obtained from Fig. 8(a). Results reconstructed from Fig. 8(b) using the (c) BG method, (d) TVBF+, (e) EDSR, and (f) ICLP.

which can be seen as a comprehensive response to spatial resolution and data integrity. The average spatial resolution of the along-track and along-scan direction is 65.8 km in the simulated 10 V/H image. However, some high-frequency information is irrecoverably lost in the data acquisition process owing to the excessively large PSF spanning multiple adjacent sampling points. Recovery of high-frequency details is a process of "creating something out of nothing." There is a limitation for the traditional deconvolution restoration method [42], [43]. It is about 45% empirically in the presence of noise.

The improvement of SRV using traditional BG methods is finite, about 41% in the average of 100 independent experiments. The TVBF+ and EDSR can upgrade SRV by 53%–58%. The ICLP achieves the most satisfactory results because of its ability to supplement high-frequency detail from other channels constantly. The SRV can be ameliorated by 76%–79%, equivalent to four to five times the original resolution. Fig. 6 shows that the ICLP result has approached the sampling interval, which means that a joint retrieval can be obtained with 89 V/H.

2) Simulated Actual Data: Admittedly, the above experiments demonstrate the effectiveness of the proposed algorithm from the perspective of simulated data. Nevertheless, the scenario we used above is comparatively straightforward and particular. A synthetic scene that closely matches the actual situation needs to be generated. Here, the actual measurements of FY3D-MWRI from December 28, 2021, are chosen. As depicted in Fig. 7, the 10-V data of the South Asia zone with 256×256 sampling points, whose geographical features include sufficient lakes, islands, and land—sea interfaces, are selected. The Tonle Sap Lake (pointed by the black arrow) and Kota Pangkalpinang (pointed by the red arrow) are magnified, respectively.

Fig. 8(b) depicts the simulated 10 V/H scene generated by Fig. 8(a) and (2). The same area as in Fig. 7 is enlarged (enclosed by the white dash-dotted rectangle) for a better visualization effect. The Sap Lake and Kota Pangkalpinang in the simulated 10 V/H scene are blurred to disappear.

Apparently, BG methods can only partially reconstruct the image and introduce drastic noise amplification. The TVBF+

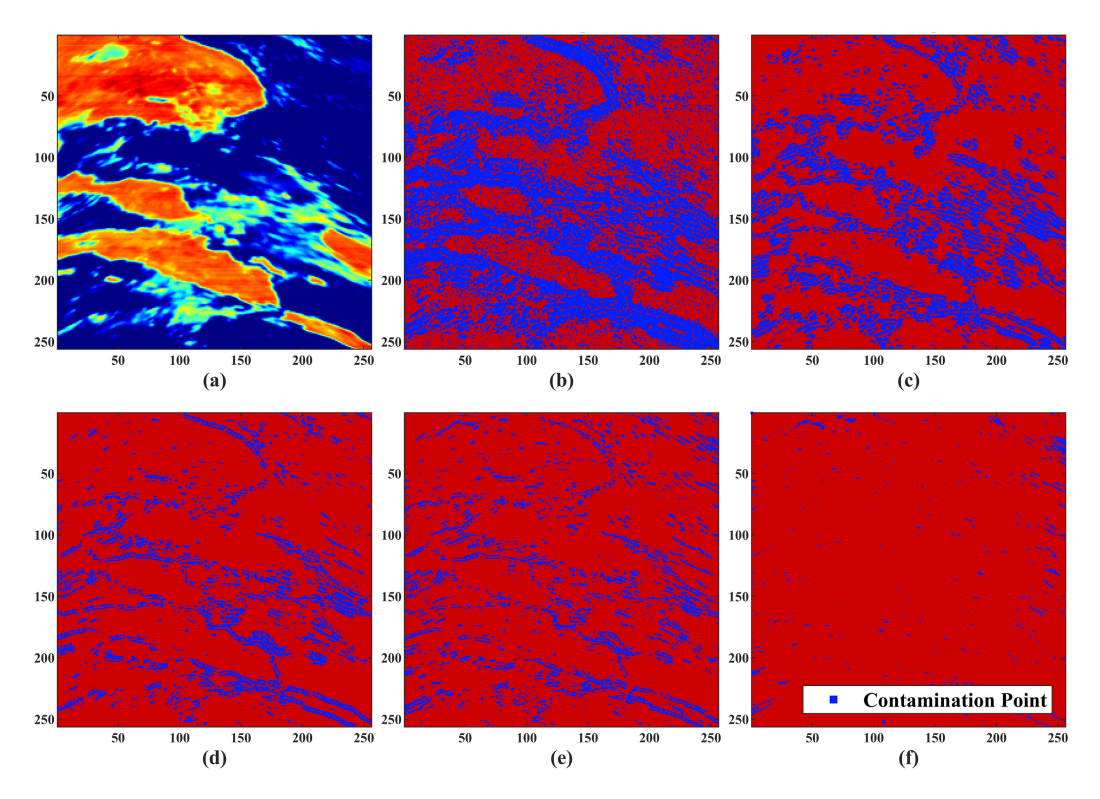


Fig. 9. (a) Synthetic scene brightness temperature image. (b) Contamination point of the simulated 10-V antenna brightness temperature image. The contamination points of the reconstructed image from Fig. 8(b) using the (c) BG method, (d) TVBF+, (e) EDSR, and (f) ICLP.

TABLE II RECONSTRUCTION PERFORMANCES OF DIFFERENT SPATIAL RESOLUTION ENHANCEMENT METHODS

Method	Scene 1			Scene 2		Average of 500 Scenes			
	PSNR	SSIM	IFOV (km)	PSNR	SSIM	IFOV (km)	PSNR	SSIM	IFOV (km)
T_B	30.5780	0.8715	65.8	33.2745	0.8990	69.2	32.2567	0.8827	67.3
BG	33.4406	0.9250	39.2	37.4097	0.9465	43.1	36.9023	0.9409	41.5
TVBF+	34.8018	0.9524	25.3	41.5247	0.9813	30.8	41.0029	0.9766	28.7
EDSR	36.9264	0.9708	21.0	42.0495	0.9829	25.5	41.4642	0.9813	24.9
ICLP	40.0489	0.9871	14.4	46.2112	0.9949	15.1	45.8972	0.9932	14.5

optimizes the data integrity problem while the accuracy of reconstructed amplitude is inadequate. The EDSR methods further improve the spatial resolution, which can be demonstrated by the clearer interface of the Kota Pangkalpinang area.

The proposed ICLP offers an outstanding performance where the amplitude and the interface of the Sap Lake and Kota Pangkalpinang are reconstructed accurately. Furthermore, almost no artifacts are introduced. The spatial resolution and data integrity are remarkably enhanced together.

The related performance metrics analysis is listed in Table II (scene 2). Additionally, 500 simulated images degraded at 10, 18, 23, and 36 V/H parameters of FY3D MWRI from December 1, 2021, to December 15, 2021, are also chosen to perform metrics evaluation. Their average results are also included in Table II.

The absolute error with the true value is of concern in the practical data application. According to the sensitivity and calibration error of the MWRI instrument [17], we set the deviation of 2.5 K to determine whether the sampling point is contaminated, as shown in Fig. 9. The contaminated sampling points in the simulated 10 V/H scene are

mainly near the land–sea interface, and there are also some contaminated sampling points in the remaining areas due to the noise. In total, about 60% sampling points in this scene are contaminated. Using the BG methods, the number of contaminated points obviously decreased by about 30%. The TVBF+ and EDSR methods ameliorate the phenomenon, and the contaminated points occur only at the land–sea transition zone. The ICLP methods eliminate most of the contaminated points (only 2.56% contaminated points left), revealing the proposed method's exceptional precise-reconstruction ability.

3) Ablation Study of Destriping Module: In fact, most of the previous spatial resolution enhancement algorithms for MWRs have largely overlooked the impact of striping noise. As shown in Fig. 10, the MWRI image was decomposed using wavelet decomposition, revealing the presence of significant stripe noise in the scanning direction of the instrument. Furthermore, the deconvolution operation also amplifies the stripe noise, as illustrated in Fig. 11.

Therefore, before applying the actual spatial resolution matching algorithm, we incorporated a stripe noise removal module (ICLP+) to ensure that the subsequent spatial

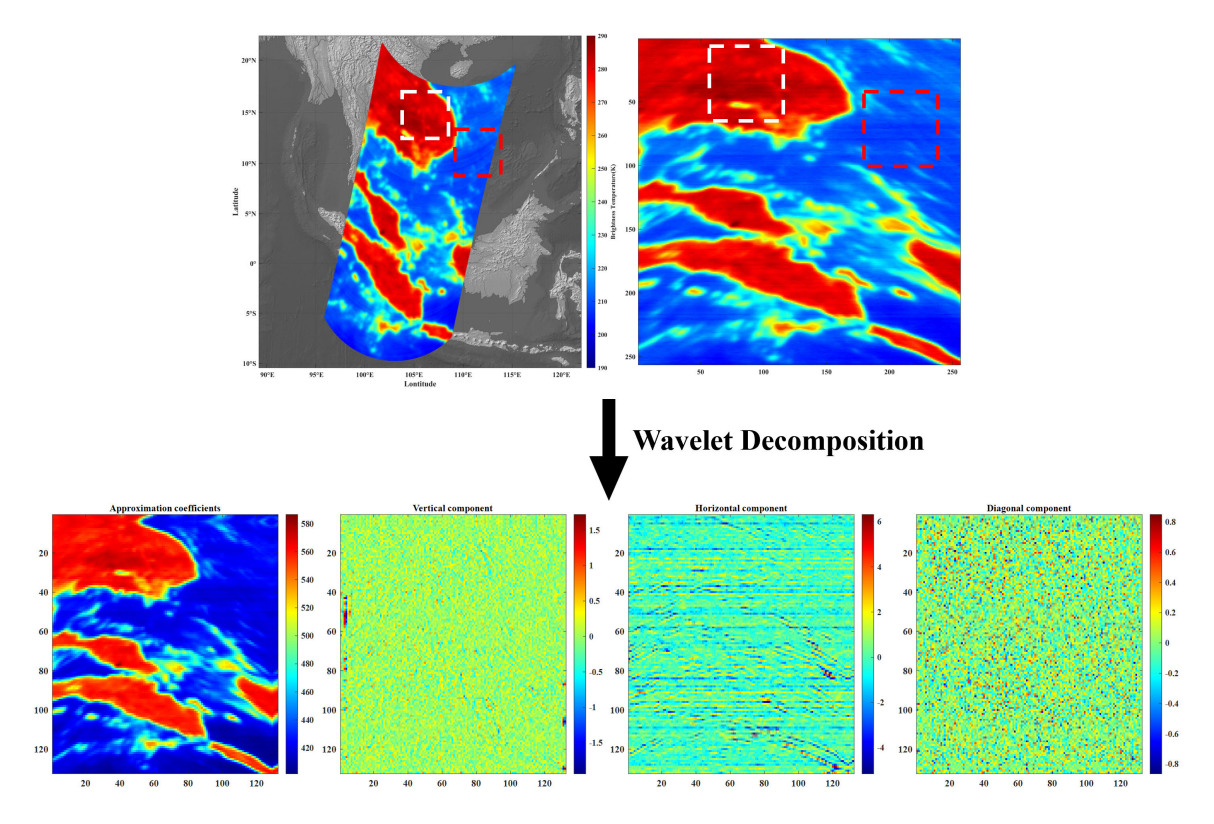


Fig. 10. Illustration of the stripe noise in the MWRI image.

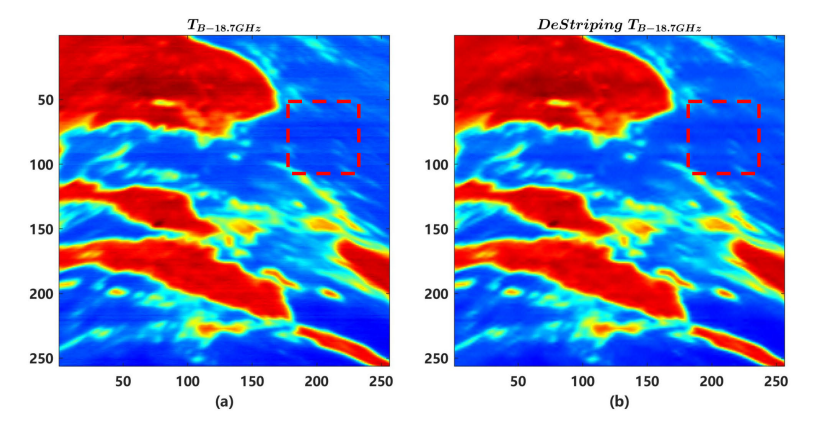


Fig. 11. Impact of the stripe noise on deconvolution.

resolution matching algorithm does not amplify the impact of stripe noise.

Based on this, we also conducted an additional ablation study. As shown in Table III, 100 typical scenes were simulated and degraded with the addition of stripe noise. The BG and ICLP methods were used for spatial resolution enhancement, and a module to remove stripe noise was added before the algorithm. The results of the ablation experiments are shown in Table III. It can be seen that in the presence of stripe noise, for the single-stage deconvolution algorithm (BG), the module for removing stripe noise before the deconvolution operation greatly improves performance. For the multistage spatial resolution enhancement algorithm (ICLP), since the algorithm itself has a denoising module, the module for removing stripe noise has a small improvement.

B. Spatial Resolution Enchantment on Actual Measurements

The above results show the superior resolution enhancement ability of the proposed ICLP method from the perspective of simulated synthetic data. In this section, the resolution enhancement effect on actual radiometer measurements is discussed.

The actual 10-V measurements are used as the experimental objects because it has the most extreme degradation condition. Since the ideal T_B at 10 V is unavailable, the actual measurements at 37 V can be used as a reference. As depicted in Fig. 12, the Tonle Sap Lake (enclosed by a white dash-dotted rectangle) and Kota Pangkalpinang (enclosed by a white dash-dotted rectangle) are not well-defined in actual 10-V measurements but are clearly presented in 36-V measurements.

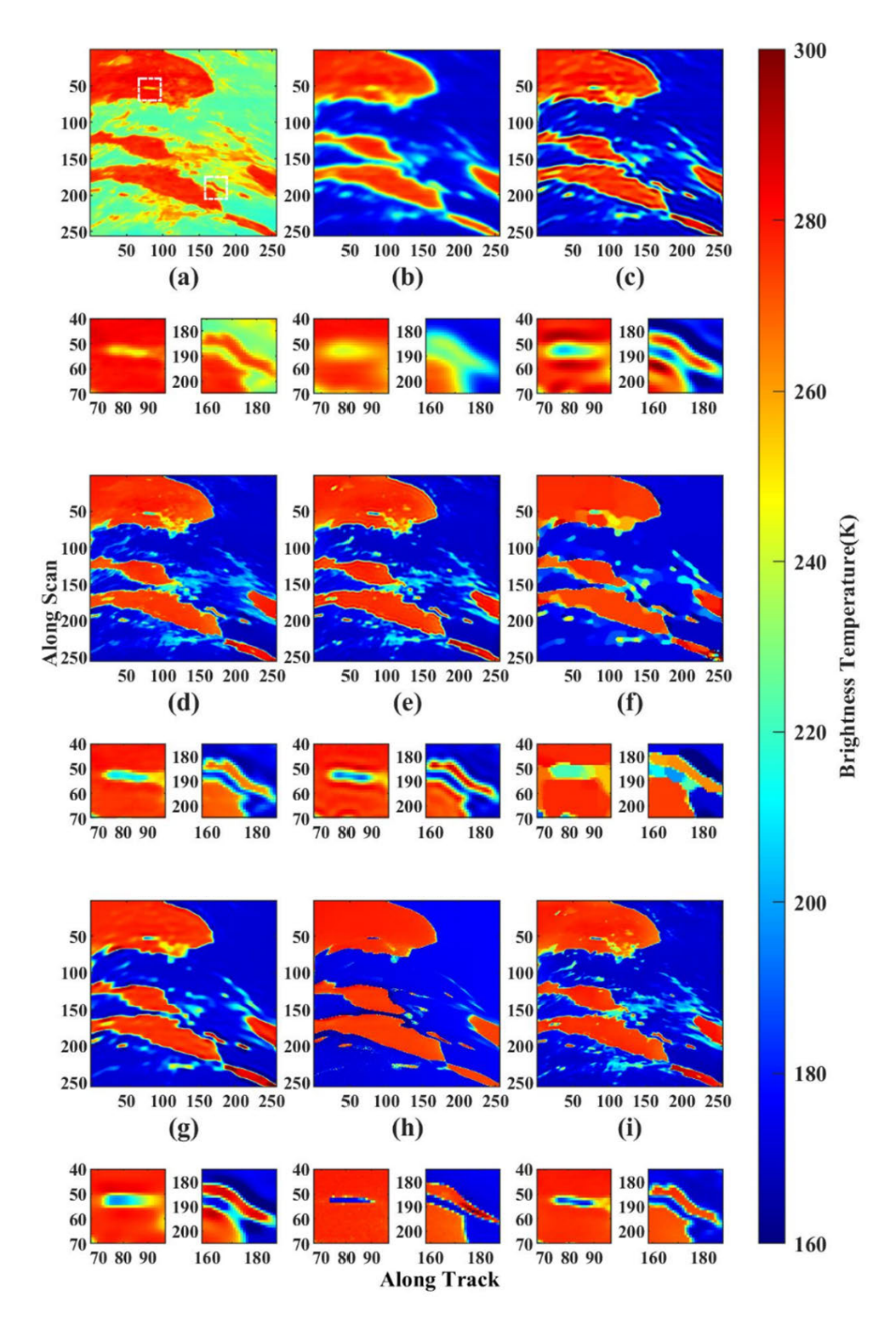


Fig. 12. (a) Actual 36-V measurements. (b) Actual 10-V measurements. Results reconstructed from Fig. 12(b) using the (c) BG method, (d) TVBF+, I EDSR, (f) PMP, (g) Outliers, (h) Real-ESRGAN, and (i) ICLP.

As shown in Fig. 12(c)–(f), all algorithms produce more precise interfaces of the lake and island. Specifically, the traditional BG algorithm resulted in poor data integrity due to amplifying noise and producing significant artifacts. The TVBF+ and EDSR methods significantly improved upon the drawbacks of the BG algorithm by reducing noise and artifacts. However, these two methods still suffer from cer-

tain limitations, including the presence of conspicuous data contamination areas in the land–sea transition zone and the inability to accurately reconstruct the amplitude of small targets such as islands and lakes. The TVBF+ method produced an over-smoothing effect due to the use of a denoising filter (Tonle Sap Lake), while the EDSR method produced an over-enhanced effect (Kota Pangkalpinang). Both over-smoothing

TABLE III

RECONSTRUCTION PERFORMANCES OF BG AND ILP W/ W/O THE DESTRIPE MODULE

	PSNR(dB)	SSIM	IFOV(km)
BG without destripe	36.1025	0.9371	42.8
BG with destripe	37.3198	0.9433	39.2
ICLP without destripe	44.9732	0.9837	15.3
ICLP with destripe(ICLP+)	45.3277	0.9848	15.2

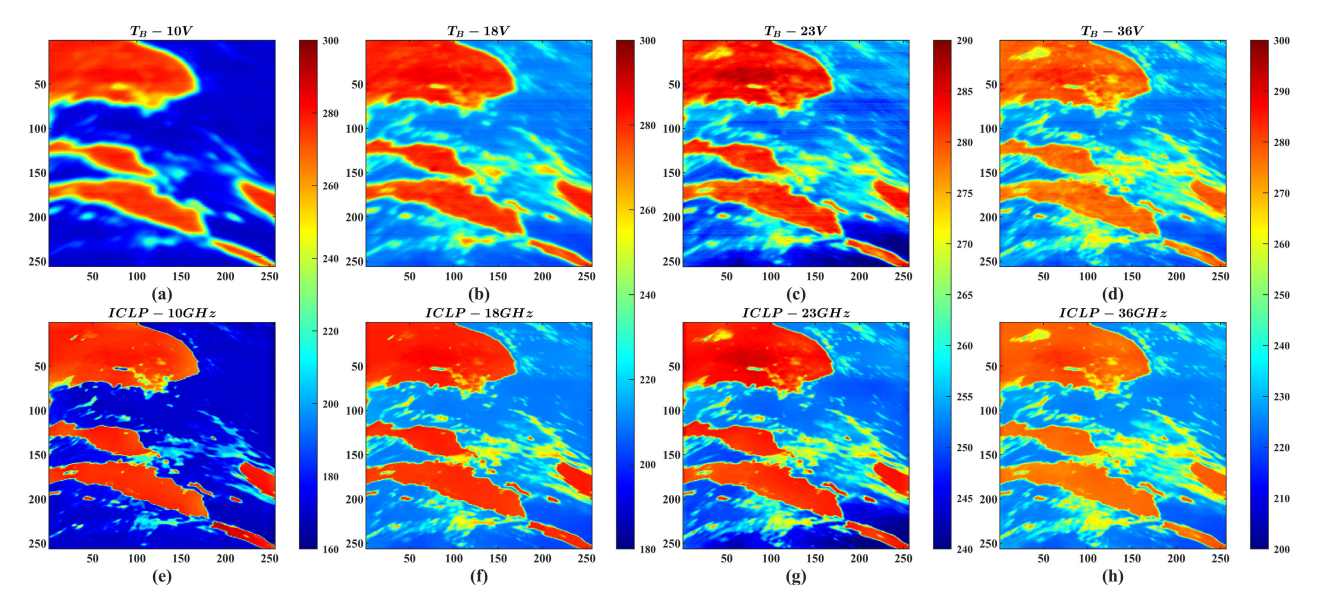


Fig. 13. (a) 10-V measurement. (b) 18-V measurement. (c) 23-V measurement. (d) 36-V measurement. Using the proposed ICLP method (e) reconstructed 10-V result, (f) reconstructed 18-V result, (g) reconstructed 23-V result, and (h) reconstructed 36-V result.

and over-enhanced effects are unacceptable as they affect the accurate acquisition of meteorological parameters for each pixel.

The PMP method effectively eliminates data contamination bands in clearly defined land-sea transition areas by using patch-wise minimal pixel prior information, but its unique prior information targeting natural images results in excessive smoothing in areas with relatively flat land/ocean gradients, causing effective information in the original image to be erased. The outliers method performs better in reconstructing the information of the land-sea boundary transition zone compared to the above-mentioned methods, but failed to accurately reconstruct the contours of islands as shown by the comparison with the 36.5-GHz channel image. The Real-ESRGAN method achieves the best restoration of land-sea gradient information, almost eliminating all land-sea transition zone polluted data, and producing almost no amplification of noise and artifacts. However, due to its GAN-based principle, the method was not completely accurate in recognizing some small structures, leading to enhancement effects beyond the original data information.

Noticeably, the proposed ICLP method effectively addressed the above issues by significantly reducing the polluted data in the land–sea transition zone, producing clearer land–sea boundaries, and generating more realistic reconstructed information when compared to the 36.5-GHz channel image with no artifacts or excessive blurring. Overall, in terms

of comprehensive consideration, the clarity of reconstructed images, reconstruction accuracy, noise amplification suppression ability, and artifact generation suppression ability, the ICLP method achieved the best reconstruction effect for the actual measured MWRI data, indicating better spatial resolution and data integrity enhancement and providing support for subsequent multichannel data spatial resolution matching.

C. Spatial Resolution Matching on Actual Measurements

We have previously demonstrated the proposed algorithm's spatial resolution enhancement capability for the most extreme 10 V/H cases. In this section, we will explore the spatial resolution-matching ability among different channels. In the actual algorithm application, we adjust the number of DD blocks to 4, 3, 3, and 2 for 10, 18, 23, and 36 V/H channels, respectively, which is due to the tradeoff between the matching accuracy and time consumption.

As shown in Fig. 13(a)–(d), the original spatial resolution increases with increasing frequency channels. Fig. 13(e)–(h) shows the spatial resolution matching results of Fig. 13(a)–(d) utilizing the proposed ICLP method. The proportion of contaminated data near the land–sea interface decreases, and the different channels' contaminated band is almost at the same level. (One thing worth noting is that because they detected various temperature brightness and atmospheric characteristics, different frequency measurements had distinct color

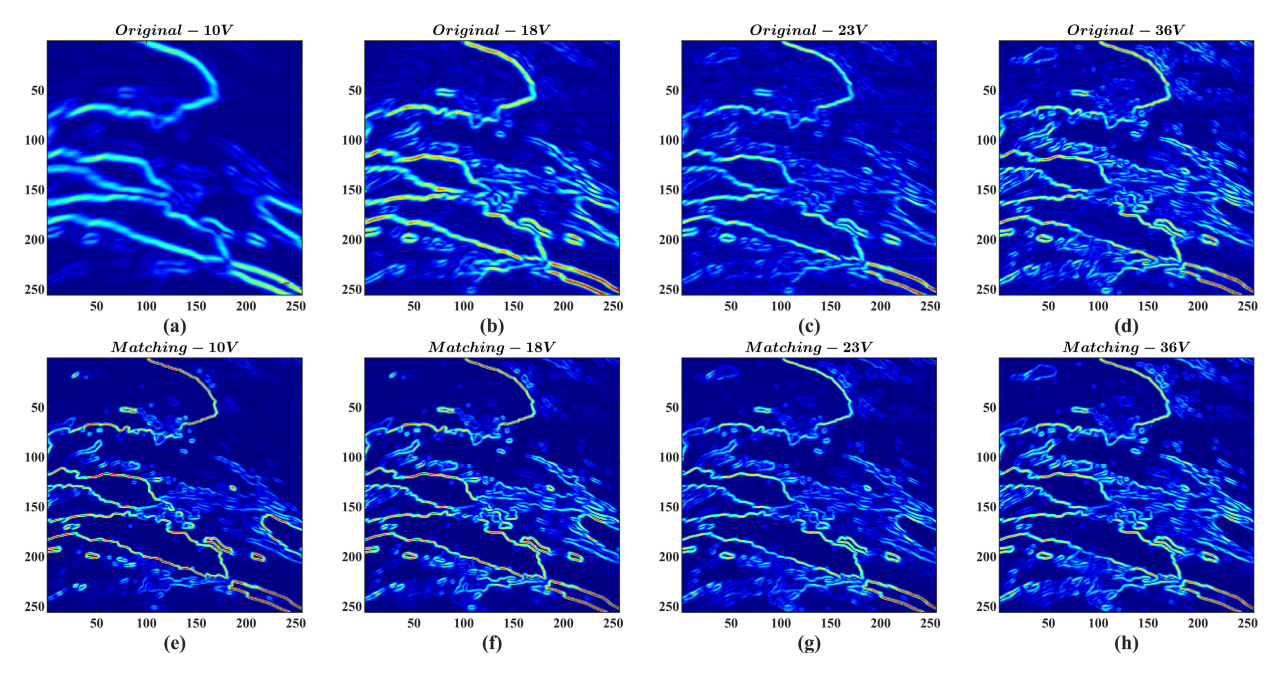


Fig. 14. (a) 10-V gradient. (b) 18-V gradient. (c) 23-V gradient. (d) 36-V gradient. Using the proposed ICLP method (e) reconstructed 10-V result, (f) reconstructed 18-V result, (g) reconstructed 23-V result, and (h) reconstructed 36-V result.

ranges. Setting the same color range would prevent certain small regions from being explicitly portrayed.)

Fig. 14 depicts the image gradients before and after applying the proposed ICLP algorithm. However, large gradients occur mainly along the land–sea interface area. The large antenna pattern footprint results in the wide gradient variation band. The width of the gradient variation band indicates the spatial resolution, which is approximated for all frequency channels after applying the spatial resolution enhancement of the proposed method. Comparing results before and after the algorithm's application reveals that ICLP achieves satisfying spatial resolution matching results.

IV. CONCLUSION

A new multichannel spatial resolution-matching technique is proposed, composed of the progressively iterative deconvolution structure and closed-loop priors mechanism. The adaptive closed-loop priors mechanism solves the mutual constraint problem of spatial resolution enhancement and noise amplification, achieving relatively high spatial resolution and data integrity. Progressive iterative deconvolution ensures that even the most severely degraded data can be progressively recovered, where high-frequency details can be well supplemented. Different levels of degraded data are recovered to the same optimal quality by setting different iterative blocks. Experimental results based on synthetic and actual MWRI measurements confirm the soundness of the ICLP method, which outperforms the traditional analytical and basic learning-based methods in restoring the small targets accurately and reducing the artifacts, especially near the land-sea interface area. The spatial resolution of all the frequency channels is matched up to a comparable level.

However, the reconstruction ability of a single sparse adaptive priors deconvolution module in ICLP is not comparable

to that of deep-learning methods. Future developments will be devoted to combining the multichannel information, the closed-loop priors mechanism, and the learning-based method to exploit the design of an effective deep explainable spatial resolution-matching network.

REFERENCES

- F. Tang, X. Zou, H. Yang, and F. Weng, "Estimation and correction of geolocation errors in FengYun-3C microwave radiation imager data," *IEEE Trans. Geosci. Remote Sens.*, vol. 54, no. 1, pp. 407–420, Jan. 2016.
- [2] Z. Yang, N. Lu, J. Shi, P. Zhang, C. Dong, and J. Yang, "Overview of FY-3 payload and ground application system," *IEEE Trans. Geosci. Remote Sens.*, vol. 50, no. 12, pp. 4846–4853, Dec. 2012.
- [3] M. A. Goodberlet, C. T. Swift, and J. C. Wilkerson, "Ocean surface wind speed measurements of the special sensor microwave/imager (SSM/I)," *IEEE Trans. Geosci. Remote Sens.*, vol. 28, no. 5, pp. 823–828, 1990.
- [4] R. Bindlish et al., "Soil moisture estimates from TRMM microwave imager observations over the Southern United States," *Remote Sens. Environ.*, vol. 85, no. 4, pp. 507–515, Jun. 2003.
- [5] X. Li, K. Zhao, L. Wu, X. Zheng, and T. Jiang, "Spatiotemporal analysis of snow depth inversion based on the FengYun-3B MicroWave radiation imager: A case study in Heilongjiang Province, China," *J. Appl. Remote Sens.*, vol. 8, no. 1, May 2014, Art. no. 084692.
- [6] C. L. Gentemann, F. J. Wentz, M. Brewer, K. Hilburn, and D. Smith, "Passive microwave remote sensing of the ocean: An overview," in *Oceanography From Space*. Dordrecht, The Netherlands: Springer, 2010, pp. 13–33.
- [7] M. P. Owen and D. G. Long, "Land-contamination compensation for QuikSCAT near-coastal wind retrieval," *IEEE Trans. Geosci. Remote Sens.*, vol. 47, no. 3, pp. 839–850, Mar. 2009.
- [8] J. X. Yang, D. S. Mckague, and C. S. Ruf, "Land contamination correction for passive microwave radiometer data: Demonstration of wind retrieval in the great lakes using SSM/I," *J. Atmos. Ocean. Technol.*, vol. 31, no. 10, pp. 2094–2113, Oct. 2014.
- [9] Y. Wang, J. Shi, L. Jiang, J. Du, and B. Tian, "The development of an algorithm to enhance and match the resolution of satellite measurements from AMSR-E," *Sci. China Earth Sci.*, vol. 54, no. 3, pp. 410–419, Mar. 2011.
- [10] J. Zhou and H. Yang, "Comparison of the remapping algorithms for the advanced technology microwave sounder (ATMS)," *Remote Sens.*, vol. 12, no. 4, p. 672, Feb. 2020.

- [11] W. D. Robinson, C. Kummerow, and W. S. Olson, "A technique for enhancing and matching the resolution of microwave measurements from the SSM/I instrument," *IEEE Trans. Geosci. Remote Sens.*, vol. 30, no. 3, pp. 419–429, May 1992.
- [12] Y. Li et al., "Spatial resolution matching of microwave radiometer data with convolutional neural network," *Remote Sens.*, vol. 11, no. 20, p. 2432, Oct. 2019.
- [13] M. Alparone, F. Nunziata, C. Estatico, F. Lenti, and M. Migliaccio, "An adaptive L^p-penalization method to enhance the spatial resolution of microwave radiometer measurements," *IEEE Trans. Geosci. Remote Sens.*, vol. 57, no. 9, pp. 6782–6791, Sep. 2019.
- [14] G. E. Backus and J. F. Gilbert, "Numerical applications of a formalism for geophysical inverse problems," *Geophys. J. Int.*, vol. 13, nos. 1–3, pp. 247–276, Jul. 1967.
- [15] D. G. Long, P. J. Hardin, and P. T. Whiting, "Resolution enhancement of spaceborne scatterometer data," *IEEE Trans. Geosci. Remote Sens.*, vol. 31, no. 3, pp. 700–715, May 1993.
- [16] F. Lenti, F. Nunziata, C. Estatico, and M. Migliaccio, "Conjugate gradient method in Hilbert and Banach spaces to enhance the spatial resolution of radiometer data," *IEEE Trans. Geosci. Remote Sens.*, vol. 54, no. 1, pp. 397–406, Jan. 2016.
- [17] H. Song, G. Wang, A. Cao, Q. Liu, and B. Huang, "Improving the spatial resolution of FY-3 microwave radiation imager via fusion with FY-3/MERSI," *IEEE J. Sel. Topics Appl. Earth Observ. Remote Sens.*, vol. 10, no. 7, pp. 3055–3063, Jul. 2017.
- [18] E. Santi, "An application of the SFIM technique to enhance the spatial resolution of spaceborne microwave radiometers," *Int. J. Remote Sens.*, vol. 31, no. 9, pp. 2419–2428, May 2010.
- [19] M. Alparone, F. Nunziata, C. Estatico, and M. Migliaccio, "A multichannel data fusion method to enhance the spatial resolution of microwave radiometer measurements," *IEEE Trans. Geosci. Remote Sens.*, vol. 59, no. 3, pp. 2213–2221, Mar. 2021.
- [20] W. Hu, W. Zhang, S. Chen, X. Lv, D. An, and L. Ligthart, "A deconvolution technology of microwave radiometer data using convolutional neural networks," *Remote Sens.*, vol. 10, no. 2, p. 275, Feb. 2018.
- [21] W. Hu, Y. Li, W. Zhang, S. Chen, X. Lv, and L. Ligthart, "Spatial resolution enhancement of satellite microwave radiometer data with deep residual convolutional neural network," *Remote Sens.*, vol. 11, no. 7, p. 771, Mar. 2019.
- [22] T. Hu, F. Zhang, W. Li, W. Hu, and R. Tao, "Microwave radiometer data superresolution using image degradation and residual network," *IEEE Trans. Geosci. Remote Sens.*, vol. 57, no. 11, pp. 8954–8967, Nov. 2019.
- [23] K. Chen, X. Fan, W. Han, and H. Xiao, "A remapping technique of FY-3D MWRI based on a convolutional neural network for the reduction of representativeness error," *IEEE Trans. Geosci. Remote Sens.*, vol. 60, 2022, Art. no. 5302511.
- [24] M. Alparone, F. Nunziata, C. Estatico, A. Camps, H. Park, and M. Migliaccio, "On the trade-off between enhancement of the spatial resolution and noise amplification in conical-scanning microwave radiometers," *IEEE Trans. Geosci. Remote Sens.*, vol. 60, 2022, Art. no. 5303714.
- [25] F. Nunziata et al., "An enhanced resolution brightness temperature product for future conical scanning microwave radiometers," *IEEE Trans. Geosci. Remote Sens.*, vol. 60, 2022, Art. no. 5301812.
- [26] W. Hu et al., "Spatial resolution and data integrity enhancement of microwave radiometer measurements using total variation deconvolution and bilateral fusion technique," *Remote Sens.*, vol. 14, no. 14, p. 3502, Jul. 2022.
- [27] A. Stogryn, "Estimates of brightness temperatures from scanning radiometer data," *IEEE Trans. Antennas Propag.*, vol. AP-26, no. 5, pp. 720–726, Sep. 1978.
- [28] T. Bonesky, "Morozov's discrepancy principle and Tikhonov-type functionals," *Inverse Problems*, vol. 25, no. 1, Jan. 2009, Art. no. 015015.
- [29] H. W. Engl, M. Hanke, and A. Neubauer, Regularization of Inverse Problems, vol. 375. Berlin, Germany: Springer, 1996.
- [30] Y. Chang, L. Yan, T. Wu, and S. Zhong, "Remote sensing image stripe noise removal: From image decomposition perspective," *IEEE Trans. Geosci. Remote Sens.*, vol. 54, no. 12, pp. 7018–7031, Dec. 2016.
- [31] H. Zhang, W. He, L. Zhang, H. Shen, and Q. Yuan, "Hyperspectral image restoration using low-rank matrix recovery," *IEEE Trans. Geosci. Remote Sens.*, vol. 52, no. 8, pp. 4729–4743, Aug. 2014.
- [32] H. E. Fortunato and M. M. Oliveira, "Fast high-quality non-blind deconvolution using sparse adaptive priors," Vis. Comput., vol. 30, nos. 6–8, pp. 661–671, Jun. 2014.

- [33] A. Levin, R. Fergus, F. Durand, and W. T. Freeman, "Image and depth from a conventional camera with a coded aperture," *ACM Trans. Graph.*, vol. 26, no. 3, p. 70, Jul. 2007.
- [34] N. Joshi, C. L. Zitnick, R. Szeliski, and D. J. Kriegman, "Image deblurring and denoising using color priors," in *Proc. IEEE Conf. Comput. Vis. Pattern Recognit.*, Jun. 2009, pp. 1550–1557.
- [35] B. Lim, S. Son, H. Kim, S. Nah, and K. M. Lee, "Enhanced deep residual networks for single image super-resolution," in *Proc. IEEE Conf. Comput. Vis. Pattern Recognit. Workshops (CVPRW)*, Jul. 2017, pp. 1132–1140.
- [36] S. Cho, J. Wang, and S. Lee, "Handling outliers in non-blind image deconvolution," in *Proc. Int. Conf. Comput. Vis.*, 2011, pp. 495–502.
- [37] F. Wen, R. Ying, Y. Liu, P. Liu, and T. Truong, "A simple local minimal intensity prior and an improved algorithm for blind image deblurring," *IEEE Trans. Circuits Syst. Video Technol.*, vol. 31, no. 8, pp. 2923–2937, Aug. 2021.
- [38] X. Wang, L. Xie, C. Dong, and Y. Shan, "Real-ESRGAN: Training real-world blind super-resolution with pure synthetic data," in *Proc. IEEE/CVF Int. Conf. Comput. Vis. Workshops (ICCVW)*, Oct. 2021, pp. 1905–1914.
- [39] H. Yang et al., "The FengYun-3 microwave radiation imager on-orbit verification," *IEEE Trans. Geosci. Remote Sens.*, vol. 49, no. 11, pp. 4552–4560, Nov. 2011.
- [40] Q. Huynh-Thu and M. Ghanbari, "Scope of validity of PSNR in image/video quality assessment," *Electron. Lett.*, vol. 44, no. 13, pp. 800–801, Jun. 2008.
- [41] Z. Wang, A. C. Bovik, H. R. Sheikh, and E. P. Simoncelli, "Image quality assessment: From error visibility to structural similarity," *IEEE Trans. Image Process.*, vol. 13, no. 4, pp. 600–612, Apr. 2004.
- [42] M. Nagorni and S. W. Hell, "Coherent use of opposing lenses for axial resolution increase. II. Power and limitation of nonlinear image restoration," J. Opt. Soc. Amer. A, Opt. Image Sci., vol. 18, no. 1, pp. 49–54, 2001.
- [43] L. B. Lucy, "Resolution limits for deconvolved images," Astronomical J., vol. 104, pp. 1260–1265, Sep. 1992.



Zhiyu Yao received the B.S. and M.S. degrees from the Beijing Institute of Technology, Beijing, China, in 2020 and 2023, respectively.

His research interests include microwave remotesensing image processing, deep learning, and its applications.



Weidong Hu was born in Shanxi, China, in 1975. He received the B.S. degree in electronics engineering and the Ph.D. degree in the electromagnetic field and microwave from the Beijing Institute of Technology, Beijing, China, in 1997 and 2004, respectively.

He is currently a Full Professor with the Beijing Key Laboratory of Millimeter Wave and Terahertz Technology, School of Integrated Circuit and Electronics, Beijing Institute of Technology. He is the author of two books. His research interests include

radar cross section measurements, microwave remote sensing, and terahertz imaging.

Dr. Hu is an Editor of the Frontiers of Information Technology and Electronic Engineering journal.



Zhiyan Feng received the B.S. degree in Internet of Things engineering from Shandong University, Qingdao, China, in 2021. She is currently pursuing the M.S. degree in electronic science and technology with the Beijing Institute of Technology, Beijing, China.

Her research interests include remote-sensing satellite simulation, data analysis, and image processing.



Wenlong Zhang received the B.E. degree from the Zhengzhou University of Light Industry, Zhengzhou, China, in 2016, and the M.S. degree from the Beijing Institute of Technology, Beijing, China, in 2018. He is currently pursuing the Ph.D. degree with The Hong Kong Polytechnic University, Hong Kong.

He has worked as a Research Assistant with the Multimedia Laboratory, Shenzhen Institute of Advanced Technology, Chinese Academy of Sciences, Shenzhen, China, from 2018 to 2020. His research interests include image super-resolution and restoration.



Zhihao Xu received the B.S. degree from Yanshan University (YSU), Qinhuangdao, China, in 2016, and the M.S. degree from the Beijing University of Technology (BJUT), Beijing, China, in 2019. He is pursuing the Ph.D. degree with the Beijing Institute of Technology (BIT), Beijing.

His research interests include terahertz radar, quasi-optical design, and signal-processing algorithms.



Leo P. Ligthart (Life Fellow, IEEE) was born in The Netherlands, in September 1946. He received the degree (cum laude) in engineering and the Ph.D. degree from the Delft University of Technology, Delft, The Netherlands, in 1969 and 1985, respectively.

Since 1988, he has been the Chair of microwave (MW) transmission, remote sensing, radar, and positioning and navigation with the Delft University of Technology. He founded the IRCTR, Delft University of Technology, where he is currently an

Emeritus Professor, a Guest Professor with universities in Indonesia and China, and the Chairperson of CONASENSE. He teaches various courses on radar and remote sensing in antennas and has published more than 650 articles, various book chapters, and books. He has supervised more than 50 Ph.D. students. His research interests include antennas and propagation, radar and remote sensing, satellite, and mobile and radio communications.

Dr. Ligthart is a member Board of Governors (BoG) of IEEE Aerospace and Electronic Systems Society (AESS), a fellow of IET, and the Academician of the Russian Academy of Transport. He is also a Founding Member of European Microwave Association (EuMA). He has chaired first EuMW in 1998. He is also an Initiated European Radar Conference (EuRAD) in 2004. He has received Honorary Doctorates at the Moscow State Technical University of Civil Aviation (MSTUCA), Moscow; Tomsk State University, Tomsk, Russia; and MTA Romania.



Yang Liu was born in Hebei, China, in 1994. He received the B.E. and Ph.D. degrees in electronics science and technology from the Beijing Institute of Technology, Beijing, China, in 2016 and 2022, respectively.

He is currently a Post-Doctoral Researcher with the Aerospace Information Research Institute, Chinese Academy of Sciences, Beijing. His research interests include radar signal processing, radar cross section measurement, and radar system design.